Axisymmetric lattice Boltzmann simulation of droplet impact on solid surfaces

Hussein N. Dalgamoni and Xin Yong

Phys. Rev. E **98**, 013102 — Published 9 July 2018

DOI: 10.1103/PhysRevE.98.013102

Axisymmetric Lattice Boltzmann Simulation of Droplet Impact on Solid Surfaces

Hussein N. Dalgamoni and Xin Yong*

Department of Mechanical Engineering, Binghamton University, The State University of New York, Binghamton, New York 13902, United States

Abstract

Droplet-solid interaction is a ubiquitous fluid phenomenon that underpins a wide range of applications. To further the understanding on this important problem, we use an axisymmetric lattice Boltzmann method (LBM) to model the droplet impact on a solid surface with different wettability. The method applies a popular free-energy LBM developed by Lee and Liu [T. Lee and L. Liu, J. Comput. Phys. **229**, 8045 (2010)] to simulate incompressible binary fluids with physical density and viscosity contrasts. The formulation is recast in cylindrical coordinates for modeling the normal impact of a three-dimensional (3D) droplet in the no-splashing regime, in which an axisymmetric flow is considered. The droplet deposits on or rebounds from the surface, governed by three key parameters: Weber number; Ohnesorge number; and equilibrium contact angle, which quantifies the surface wettability. We elucidate the distinct impact dynamics by probing droplet morphology and contact line behavior in great detail, which are quantitatively characterized by spreading factor, droplet aspect ratio, and dynamic contact angle. The simulations also resolve fluid velocity field inside and outside the droplet, which provides additional insight into the morphological evolution and mass/momentum transfer during impact. Explicit comparison between axisymmetric and conventional 2D LBM highlights the importance of axisymmetric terms in governing equations for reproducing physical impact behavior. The axisymmetric LBM significantly reduces computational cost as compared with 3D LBMs and offers an effective means to study droplet impact in applicable conditions.

*E-mail: xyong@binghamton.edu

1. Introduction

Droplet impact on solid surfaces is one of the fundamental phenomena encountered in a wide range of important engineering processes, such as spray cooling, inkjet-based additive manufacturing, anti-fouling and anti-corrosion paints and coatings [1,2]. In these applications, the dynamic behavior of the droplet as a result of its interaction with a solid surface plays a critical role in determining cooling efficiency, printing resolution, and coating performance. Therefore, understanding droplet impact dynamics is of great significance in many technological advances. In general, droplet impact on a solid surface comprises an initial spreading phase governed by inertia force, and a recoiling phase governed by surface tension and viscous forces [3–5]. Droplet dynamics during spreading and recoiling is determined by droplet properties, impact velocity and angle, and surface wettability and roughness [6]. Varying these parameters could lead to distinct impact outcomes, which range from deposition, partial rebound, complete rebound, to splashing [1–6].

As the interests of droplet impact shift toward miniaturized scale, complex fluid compositions, and nanoengineered novel surfaces in the past decades [7–19], fluid experiments to resolve fast and intricate impact dynamics for these new systems are challenging. The computational fluid dynamics (CFD) modeling complements advanced experimental techniques and provides unique insight into hydrodynamics. Using the volume of fluid, front-tracking, or level set methods [20,21], the simulations have been quite successful in studying multiphase flow problems with complex geometries. Although these techniques offer an important visualization of fluid interface evolution and detailed flow field in a wide parameter space, they generally suffer from numerical complications when explicitly tracking highly deformed interfaces during droplet impact [20,21].

As an efficient numerical method for fluid dynamics, the lattice Boltzmann method (LBM) has evolved rapidly in the last two decades [22]. Unlike the conventional CFD methods that solve the Navier-Stokes (N-S) equations based on the macroscopic continuum assumption, the LBM can accurately simulate macroscopic fluid behavior based on a microscopic perspective of fluid systems. In the LBM, one solves the kinetic equations of appropriate statistical particle distribution functions (PDFs) from which the macroscopic variables, such as density, velocity, and pressure, can be obtained by evaluating the hydrodynamic moments of these PDFs [23,24]. Several LBMs have emerged for simulating multiphase and/or multicomponent flows [25].

However, any density and viscosity ratios between the two fluid phases inevitably cause numerical instabilities [20,21,25]. The ability to simulate liquid-gas systems with physical density and viscosity contrasts is central to the development of multiphase LBM. Recently, this issue has been addressed in the free energy approach [26–29] based on more efficient numerical schemes, e.g., stable discretization and multi-relaxation time [30–33].

The LBM is commonly formulated in Cartesian coordinates. However, many multiphase flow problems possess axisymmetry in nature, such as head-on droplet collision, normal impact of droplet on flat surfaces without splashing, and Rayleigh-Plateau instability of liquid jets. By adopting the intrinsic rotational symmetry in these problems, the axisymmetric LBM that depends on only two coordinates can capture accurate 3D hydrodynamics, which is more computationally efficient than 3D LBM. However, the application of axisymmetric LBM receives much less attention than the conventional 2D and 3D LBMs. Halliday et al. [34] presented the first axisymmetric model by introducing forcing terms into the microscopic evolution equation of LBM. Using the Chapman-Enskog expansion as in the original LBM, Halliday et al. [34] recovered the macroscopic continuity and momentum equations in axisymmetric cylindrical coordinates. Premnath and Abraham [35] then applied the axisymmetric implementation to multiphase flow. In their model, the forcing terms that represent the axisymmetric contribution of inertial, viscous, and surface tension forces, as well as the order parameter of fluid phases, were added to the standard multiphase lattice Boltzmann equations (LBEs). Mukherjee and Abraham further improved the method for systems with density contrasts and applied it to study droplet impact on wet [30] and dry walls [36]. Recently, Sun et al. [37] extended the Lee and Liu model [32] to axisymmetric multiphase flow with large density and viscosity contrasts and simulated head-on droplet collision. Despite these developments and applications, the normal impact of a droplet on a solid surface with significant density and viscosity ratios has not been comprehensively studied using the axisymmetric LBM.

This paper presents numerical simulations of droplet impact with low computational cost, which use the axisymmetric LBM capable of achieving physical density and viscosity ratios across the liquid-gas interface. We validate the axisymmetric model against previous experiments and simulations of head-on droplet collision and droplet impact on solid surfaces. We comprehensively investigate the effects of Weber number, Ohnesorge number, and surface wettability on the dynamic behavior of the droplet during its interaction with the solid substrate.

Below, we briefly describe the axisymmetric LBM with density and viscosity contrasts that represents the physical liquid-gas coexistence and its numerical implementation in Section 2. Section 3 presents the simulation results of droplet impact with respect to the three governing parameters. Conclusions are drawn in Section 4.

2. Numerical Method

2.1 Multiphase Lattice Boltzmann Method for Axisymmetric Flows

The multiphase LBM used in this study is based on the free energy formulation, which is essentially a phase field approach. In the presence of solid substrate, the total free energy of the system includes the bulk free energy and the interfacial free energy of the binary fluid, as well as the surface integral of the free energy density that describes the interactions between the liquid-gas interface and a solid substrate. Overall, it is given by

$$\psi_{\text{total}} = \int_V \left(E_0(C) + \frac{\kappa}{2}|\nabla C|^2 \right) dV + \int_S \left(\phi_0 - \phi_1 C_s + \phi_2 C_s^2 - \phi_3 C_s^3 \right) dS \tag{1}$$

The bulk free energy $E_0(C) = \beta C^2 (C-1)^2$ depends on fluid composition C, which is defined as the ratio of the local density to the bulk density of the liquid phase. Its value varies between 0 in the gas phase to 1 in the liquid phase. β is a constant that determines the potential barrier separating two immiscible phases. The second term in the volume integral represents the interfacial free energy with κ being the gradient parameter. At thermodynamic equilibrium, the total free energy of the binary fluid is minimized, which drives the phase separation. This leads to a constant chemical potential $\mu = \partial E_0 / \partial C - \kappa \nabla^2 C$. The equilibrium profile of a planar liquid-gas interface at equilibrium is $C(z) = 0.5 + 0.5\tanh(2z/\xi)$, where z is the coordinate normal to the interface and ξ dictates the interfacial thickness. Given ξ and β, the gradient parameter and the interface tension can be calculated respectively as $\kappa = \beta\xi^2/8$ and $\sigma = \sqrt{2\kappa\beta}/6$ [32].

The surface integral is introduced to model the wetting behavior, in which C_s is the composition at the solid surface S [32]. The cubic wetting boundary condition [32,38] with $\phi_0 = \phi_1 = 0$, $\phi_2 = 1/2\phi_c$, and $\phi_3 = 1/3\phi_c$ is adopted in this study to avoid negative equilibrium density on a non-wetting surface, where ϕ_c is a constant related to the value of equilibrium

contact angle θ^{eq}. θ^{eq} is defined by Young's equation as $\cos\theta^{eq} = \left(\sigma_{sg} - \sigma_{sl}\right)/\sigma_{lg} = -\Omega_c$, where σ_{sg}, σ_{sl} and σ_{lg} are the interfacial tension for solid-gas, solid-liquid, and liquid-gas, respectively, and $\Omega_c = \phi_c/\sqrt{2\kappa\beta}$ is the dimensionless wetting potential. The equilibrium contact angle is achieved when $\mathbf{n}\cdot\nabla C|_S = \left(\phi_c/\kappa\right)\left(C_s - C_s^2\right)$ is fulfilled at the solid surface [32,38].

Based on the free energy functional, the hydrodynamics of binary fluid is described by the Cahn-Hilliard, continuity, and momentum equations, which are written in axisymmetric cylindrical coordinates, respectively as [25,39]

$$\frac{\partial C}{\partial t} + \left(u_z\frac{\partial C}{\partial z} + u_r\frac{\partial C}{\partial r}\right) + C\left(\frac{\partial u_z}{\partial z} + \frac{\partial u_r}{\partial r}\right) = M\left(\frac{\partial^2\mu}{\partial z^2} + \frac{\partial^2\mu}{\partial r^2}\right) + \frac{M}{r}\frac{\partial\mu}{\partial r} - \frac{Cu_r}{r} \tag{2}$$

$$\frac{\partial\rho}{\partial t} + \left(u_z\frac{\partial\rho}{\partial z} + u_r\frac{\partial\rho}{\partial r}\right) + \rho\left(\frac{\partial u_z}{\partial z} + \frac{\partial u_r}{\partial r}\right) = -\frac{\rho u_r}{r} \tag{3}$$

$$\rho\left[\frac{\partial u_z}{\partial t} + u_z\frac{\partial u_z}{\partial z} + u_r\frac{\partial u_z}{\partial r}\right] = -\frac{\partial P}{\partial z} + \eta\left(\frac{\partial^2 u_z}{\partial z^2} + \frac{\partial^2 u_r}{\partial r^2}\right) + \frac{\eta}{r}\frac{\partial u_z}{\partial r} - \frac{u_z u_r}{r} \tag{4}$$

$$\rho\left[\frac{\partial u_r}{\partial t} + u_z\frac{\partial u_r}{\partial z} + u_r\frac{\partial u_r}{\partial r}\right] = -\frac{\partial P}{\partial r} + \eta\left(\frac{\partial^2 u_z}{\partial z^2} + \frac{\partial^2 u_z}{\partial r^2}\right) + \frac{\eta}{r}\frac{\partial u_r}{\partial r} - \frac{\eta u_r}{r^2} - \frac{u_r u_r}{r} \tag{5}$$

ρ is the local fluid density, which varies across the interface. u_r and u_z are fluid velocities in the radial and axial directions, respectively. P is the hydrodynamic pressure, η is the dynamics viscosity, μ is the chemical potential, and M is the mobility constant that has positive values.

Following the Lee and Liu method detailed in Ref. [32], the above governing equations can be discretized and solved numerically by the lattice Bhatnagar-Gross-Krook (BGK) model using two PDFs. An incompressible transformation is applied to address the numerical instability induced by large density and viscosity contrasts [33,40]. To properly recover the macroscopic equations, the axisymmetric terms present in the corresponding discrete Boltzmann equations as additional forcing terms, and the definitions of fluid macroscopic properties based on PDFs are modified [34,35,37]. The l'Hopital's rule is applied for terms such as $\frac{Cu_x}{x}$ or $\frac{1}{x}\frac{\partial\mu}{\partial x}$ to avoid singularity at the axis of symmetry ($x = 0$) [25]. A detailed description and derivation of the method can be found in Refs. [32,37].

The D2Q9 lattice velocity scheme is employed in this study. A schematic plot of the computational domain with grid size 360×360 is shown in Figure (1). The impact axis of a spherical droplet with radius $R_0 = 60$ coincides with the left boundary of the domain. The bottom boundary is the solid substrate, where the standard bounce-back rule is imposed after the streaming step [32,38]. Consistent with the axisymmetric assumption, symmetric bounce-back boundary conditions are imposed at the left boundary after the streaming step. No-flux boundary conditions are applied on the top and right boundaries, where zero gradients normal to the boundary are fulfilled for all of the macroscopic variables.

Ranging from smooth spreading to splashing, jetting or rebound, outcomes of droplet impact on a solid surface depend critically on impact parameters and solid surface properties. The dynamic interaction between droplet and surface is governed by the interplay of inertia, viscous, and surface tension forces. Because splashing generates secondary droplets, which break the rotational symmetry along the impact axis, we limit the study to the no-splashing regime by imposing small impact velocity. The impact velocity of the droplet U_0 is set based on the Weber number ($\mathrm{We} = 2\rho R_0 U_0^{\,2}/\sigma$) in each impact simulation. To study the viscous dissipation effect, we vary the Ohnesorge number ($\mathrm{Oh} = \eta_\mathrm{l}/\sqrt{2\rho_\mathrm{l} R_0 \sigma}$). Unless otherwise stated, the density ratio of the liquid droplet to the ambient gas is $\rho_\mathrm{l}/\rho_\mathrm{g} = 842$ and the corresponding dynamic viscosity ratio is $\eta_\mathrm{l}/\eta_\mathrm{g} = 181$. The interfacial tension and thickness are fixed at $\sigma = 0.002$ and $\xi = 5$, respectively. For each impact, the mobility is varied such that the Peclet number ($\mathrm{Pe} = U\kappa^{1/2}/M\beta^{3/2}$) is kept constant at $\mathrm{Pe} = 10$.

To characterize impact dynamics, we measure the spread factor D^*, aspect ratio H^*, and dynamic contact angle θ^{dyn}. The spread factor is defined as $D^* = D/D_0$, where D_0 is the initial droplet diameter before contact. D is the instantaneous blob diameter during spreading, but becomes the diameter of wetted area during recoiling. The aspect ratio is defined as $H^* = H/D_0$ with H representing the droplet height measured at the axis of symmetry. The dynamics contact angle measured by the fluid composition gradient as $\theta^{\mathrm{dyn}} = \tan^{-1}\left(\partial_z C/\partial_r C\right)$. The composition gradients $\partial_r C$ and $\partial_z C$ at the contact line are taken as the average value over the interfacial

thickness. To study the effect of certain parameters, we vary the one of interest while keep others constant.

As the problem is reduced to two dimensions with fewer discretized velocities (D2Q9 versus D3Q27 [32]), the axisymmetric model offers at least two orders of magnitude improvement in computational efficiency even with additional overhead for calculating axisymmetric forcing terms. This allows one to simulate bigger droplets and provides better resolutions for the dynamics of the diffuse interface in the free energy LBM. All simulation results are generated by a serial C code. A typical simulation includes an equilibrium stage of 50,000 timesteps and an impact stage, which ranges from 40,000 to 150,000 timesteps, depending on the impact conditions. The total simulation takes 40 to 66 hours on a 3.3 GHz processor.

2.2 Model Validation

To validate the axisymmetric LBM, we conduct a benchmark simulation of normal droplet impact on a hydrophobic surface and compare the results with previous experiments and 3D LBM simulations [4,32]. The impact conditions are matched by assigning the same dimensionless numbers We = 103 and Oh = 0.015. The same as the 3D LBM simulations, a density ratio of 842 is considered for the glycerin/water mixture used in the experiments [4]. Due to numerical stability limitation, our benchmark has a slightly higher viscosity ratio $\eta_l/\eta_g = 93.5$ (51 in the previous studies). The interfacial tension and thickness are selected to be $\sigma = 0.004$ and $\xi = 5$. Figure (2) compares the variations of the spreading factor and the aspect ratio during impact. D^* in the axisymmetric benchmark shows excellent agreement with both experiments and 3D simulations. H^* exhibits notable deviations from the experimental results in the late stage of impact. By closely examining the experimental images (Figure 2 in Ref. [4]), we attribute this discrepancy to the partial rebound in the experiment, which left a small residual droplet on the surface. In contrast, the droplet completely rebounded in our simulation. We speculate the partial rebound is caused by contact angle hysteresis induced by surface roughness, which is not considered in the simulations.

3. Results and Discussion

3.1 Effect of Weber Number

The Weber number characterizes the relative magnitude of the kinetic energy (inertia) to the surface tension energy. Figure (3) shows sequential morphologies of droplet impinging at two different We numbers (We = 20 and 96) with the fixed Oh number (Oh = 0.0218). The starting time is defined when the droplet makes contact with the solid surface. Even in the early stage, i.e., at T = 0.6, distinct morphologies are apparent. On the hydrophobic surface, the front of the spreading lamella detaches from the substrate for droplet with high impact velocity. This levitated lamella is induced by the lubrication force in air trapped under the droplet front, which results from the rapid movement of contact line and the large advancing contact angle [1–3]. The morphology difference becomes more pronounced as impact proceeds. At T = 1.2, the droplets on the hydrophobic surface almost finish their spreading regardless of We number, while the ones on the hydrophilic surface spread further. The recoiling occurs significantly later on the hydrophilic surface. The comparison of subsequent snapshots shows faster recoiling on the hydrophobic surface due to much lower surface friction. In the recoiling stage, the droplet with We = 20 undergoes a few cycles of oscillations until it deposits with a steady shape defined by equilibrium contact angle, while the rapid recoiling of We = 96 droplet eventually leads to complete rebound from the surface. In contrast, the We number does not change the outcome of impact on the hydrophilic surface. Both cases deposit, with the same final shape.

A systematic study of the We number effect is performed for We number between 12 and 150 at a constant Oh number (Oh=0.0218). Figure (4) plots droplet spreading factor, aspect ratio, and dynamic contact angle against non-dimensional time ($T = U_0 t / D_0$) on the two surfaces, where t is the simulation time. On the hydrophilic surface, both D^* and H^* vary quickly in the early impact until reaching a maximum value (see Figure (4a)). The maximum spreading factor increases with a higher We number because greater impact inertia induces larger deformation. The minimum aspect ratios have similar values for different We numbers. All spreading factors then decrease gradually to the same equilibrium value. In contrast, the aspect ratio maintains at the minimum for a notable period of time, which represents the universal lamella film for all impact conditions and wetting properties [41–43]. The droplet with a higher We number requires more time to reach equilibrium due to significant spreading. The initial spreading is similar on the hydrophobic surface, which indicates the surface wettability has negligible influence on the early impact. However, the maximum spreading factor is notably smaller for the same We number. Furthermore, Figures (4b) and (4d) highlight the damped oscillations toward the

equilibrium value for the droplets with $We \leq 22$. D^* monotonically reduces to zero when $We \geq 54$, which corresponds to complete rebound.

In Figure (4e), dynamic contact angles exhibit rapid decreases at the beginning of impact on the hydrophilic surface. The droplets with We = 96 and 150 show a kink in the θ^{dyn} evolution, where a local minimum value is reached, followed by an immediate increase. This unique behavior can be attributed to the inertia transfer from the normal direction to the transverse direction during spreading. The significant inertia transfer at high We number causes excess reduction of θ^{dyn} compared with low We number droplets, whose dynamics is dominated by the liquid-solid surface energy. θ^{dyn} s of different droplets that eventually converge and the values monotonically decrease to a global minimum smaller than the equilibrium contact angle θ^{eq}. During the recoiling, the apparent receding contact angle remains almost unchanged. The dynamic contact angle finally approaches θ^{eq} as the contact line receding stops. On the hydrophobic surface, the dynamic contact angle shows much more complex variations as shown in Figure (4f). In particular, θ^{dyn} of the droplet with $We \geq 54$ has multiple kinks in the spreading stage. The primary kink that occurs at the end of spreading stage is associated with the formation of the levitated lamella, during which the dynamic contact angle increases. After that, the dynamic contact angle decreases again as the lamella vanishes. In the recoiling stage, θ^{dyn} increases toward the equilibrium value 110° until complete rebound occurs (θ^{dyn} undefined afterward). In contrast, in the cases of $We \leq 54$, θ^{dyn} decreases monotonically without the kinky behavior during spreading, but undergoes dramatic oscillations toward the equilibrium value when recoiling. The oscillations lead to variation of θ^{dyn} between advancing and receding contact angles.

From an energetic point of view, the remaining inertia of impact after viscous dissipation and conversion to liquid-solid surface energy does not overcome the liquid-gas interfacial energy regardless of surface wettability. Thus, the droplet preserves structural integrity throughout impact. For the hydrophilic surface, wider droplet spreading consumes more kinetic energy. Therefore, the recoiling is dominated by the interfacial surface tension of the deformed droplet and surface wettability, which drives all droplets to the same equilibrium morphology. On the hydrophobic surface, a droplet with low We number does not entail sufficient inertia that can exceed the total surface energy of wetted area, which leads to deposition after oscillations.

Conversely, large inertia at high We number effectively overcomes viscous dissipation and substrate surface tension, which leads to complete rebound from the hydrophobic surface.

3.2 Effect of Ohnesorge Number

Figure (5) shows the shape evolution of a droplet that impacts at two different Oh numbers (Oh = 0.0218 and 0.074) with the fixed We number (We = 20). Here, we apply a relatively low We number to focus on the deposition regime on both substrates. The results indicate that Oh number influences only dynamics, but does not alter impact outcomes and the final equilibrium shape. We vary the Oh number between Oh = 0.0196 and 0.074 while keeping the We number fixed We = 20 to comprehensively probe the Oh number effect on impact dynamics. On the hydrophilic surface, the maximum D^* increases as the Oh number reduces due to less viscous dissipation. An overdamped behavior without the recoiling stage is observed at Oh = 0.074, as shown in Figure (6a). The dynamics of droplet impact closely resembles the free vibration of a damped spring-mass system [44–46]. This analogy is even more prominent for impact on the hydrophobic surface. Figure (6b) confirms that the damping effect is inversely proportional to the Oh number. The lowest Oh number $\mathrm{Oh} = 0.0196$ results in complete rebound. The droplet aspect ratio in Figure (6c) reveals a secondary maximum for Oh = 0.052 and 0.074, and the dynamic contact angle curves in Figure (6e) show kinks. From the velocity field in Figure (7), we find that the fluid at the droplet center is reflected back by the substrates and pushes the droplet surface to rise temporarily. This behavior is caused by the dominated viscous forces, which hinder droplet spreading and drive an upward flow. The oscillatory behaviors of spreading factor, aspect ratio, and dynamic contact angle on the hydrophobic surface are coordinated. The oscillation frequency and magnitude during the recoiling stage are inversely correlated with the Oh number.

Regardless of surface wettability, the strong viscous effect quickly dissipates kinetic energy of impact, which leaves the droplet governed by the surface tension toward thermodynamic equilibrium. On the other hand, weak viscous forces at a small Oh number demand longer time (and more cycles of oscillations) to dissipate kinetic energy until the surface tension takes effect. In all, the droplet can reach an equilibrium state if enough energy is dissipated during initial spreading; otherwise, it will start recoiling with sufficient energy to partially/completely rebound.

To provide deeper insight into the Oh number effect, Figure (8) shows the time evolution of the total kinetic energy and the total viscous dissipation energy of the droplet, both normalized by its initial kinetic energy. The normalized total kinetic energy (KE*) of the droplet is calculated by the summation of the instantaneous kinetic energy over liquid lattice sites $\mathrm{TKE} = \pi \sum_i \sum_j \rho_l x_{i,j} \left| \mathbf{u}_{i,j} \right|^2$ divided by the initial kinetic energy $\mathrm{IKE} = \pi \sum_i \sum_j \rho_l x_{i,j} U_0^2$. Here, (*i, j*) represents the indices of liquid lattice site. The normalized total viscous dissipation energy (DE*) is calculated from the viscous dissipation rate ϕ per unit volume, which is defined as

$$\phi = 2\eta \left\{ \left(\frac{\partial u_r}{\partial r} \right)^2 + \left(\frac{\partial u_z}{\partial z} \right)^2 + \left(\frac{u_r}{r} \right)^2 \right\} + \eta \left(\frac{\partial u_r}{\partial z} + \frac{\partial u_z}{\partial r} \right)^2 - \frac{2}{3} \eta \left(\frac{1}{r} \frac{\partial (r u_r)}{\partial r} + \frac{\partial u_z}{\partial z} \right)^2 \qquad (6)$$

Using Equation (6), we calculate $\phi_{i,j}$ for each lattice site inside the liquid phase and obtain the total viscous dissipation rate $\mathrm{VDR} = 2\pi \sum_i \sum_j x_{i,j} \phi_{i,j}$. Finally, DE* is obtained by numerical integral of VDR in time after impact and subsequently normalized by IKE. Notably, the total viscous dissipation energy considers only contribution from the viscous flow inside the droplet. Other mechanisms of dissipation such as contact line dissipation and viscous dissipation in the rim [47] are not included.

On the hydrophilic surface (Figure (8a)), we observe that KE* first decreases until a local minimum is achieved. With the increase of Oh number, this minimum is reached earlier and its value increases. Then all KE* curves increase again toward a local maximum, which also occurs earlier with increasing magnitude for a higher Oh number. Finally, KE* decreases to zero, which indicates a static droplet. On the other hand, DE* increases quickly in the early stage of impact and approaches a nearly constant value that is weakly dependent on Oh number. According to conservation of energy, the kinetic energy change equals viscous dissipation energy and surface energy change. Since the simulations with three different Oh numbers all reach the same equilibrium state after deposition, the viscous dissipation energy should be the same across these simulations. The small differences of DE* shown in Figure (8) indicate other types of viscous dissipation may play a role here.

The secondary maxima of KE* curves are one order of magnitude higher for the hydrophobic surface. This is because the maximum spreading factor on the hydrophobic surface is always lower than that on the hydrophilic surface. Thus, less energy is transferred to and stored as the interfacial and surface energies. In addition, less time is available to viscous

dissipation. Overall, the droplet can recoil with more kinetic energy. If the inertia is sufficient to overcome other forces in recoiling, a complete rebound occurs; otherwise the droplet deposits on the surface after oscillations.

3.3 Effect of Equilibrium Contact Angle

The effect of surface wettability on the droplet dynamics is shown in Figure (9). We explore a θ^{eq} range from 30° for 110°. The maximum spreading increases with enhanced surface wettability. For $\theta^{eq} \leq 50^{o}$, the spreading factor decreases gradually to θ^{eq} in the recoiling stage, while it oscillates for $\theta^{eq} > 50^{o}$. The frequency and magnitude of the oscillations are inversely correlated with the surface wettability. Figure (9b) shows the aspect ratio minima reached in the spreading phase are independent of θ^{eq}, but the oscillations for $\theta^{eq} > 40^{o}$ are amplified as θ^{eq} increases. In Figure (9c), the dynamic contact angle shows a gradual and smooth decrease toward the equilibrium contact angle when $\theta^{eq} = 30^{o}$ and 40^{o}. For $\theta^{eq} \geq 50^{o}$, the dynamic contact angle decreases gradually, then oscillates slightly toward θ^{eq}.

3.4 Velocity Vector Field

During droplet spreading and recoiling, the velocity vector field inside the droplet and in the gas phase, which surrounds the droplet, exhibits remarkable changes. These changes in fluid velocity influence energy dissipation and thereby determine the outcome of impact. The most dramatic changes in the flow field are associated with the droplet impact on the hydrophobic surface at high We number as shown in Figure (10). As the droplet approaches the solid surface, a radial moment of the gas adjacent to the solid surface starts to build up. After the spreading begins, a radial velocity also develops in the liquid phase. At T = 0.57, a counterclockwise circulation in the gas phase can be observed above the levitated lamella of the droplet. After the maximum spreading is reached, the fluid velocity near the outer rim of the droplet reverses direction, while the flow above the stable lamella film continues to move outward. As a result, two opposite circulatory flows are created at T = 2.30. As the backward flow strengthens during recoiling, both flows in the droplet and the surrounding gas point inward and a clockwise circulation appears in the snapshot of T = 3.60. At T = 5.60, the liquid inside the droplet is now moving upward and parallel to the axis of symmetry, which eventually drives the complete rebound of the droplet from the surface.

3.5 Axisymmetric LBM versus 2D LBM

To highlight the effect of axisymmetric terms to a pure 2D LBM, Figure (11) compares the time sequences of droplet shapes when impacting on the hydrophobic surface ($\theta^{eq} = 110^{\circ}$) at We = 150 and Oh = 0.0218. The droplet morphologies start to deviate from each other at the early stage of impact. The droplet in the 2D simulation spreads approximately two times more than that in the axisymmetric simulation at T = 1.92. By T = 4.0, the axisymmetric droplet starts recoiling, while the 2D droplet still undergoes spreading. The axisymmetric droplet completely rebounds from the surface at T = 18.85, while the 2D droplet is still in the recoiling stage. Most importantly, the final impact outcome is completely different: the axisymmetric droplet completely rebounds and the 2D droplet deposits on the solid surface. This comparison indicates that the surface tension effect is significantly underestimated in the 2D simulation, which results in unphysical impact dynamics for a 3D droplet.

4. Conclusions

In this study, droplet impact on a flat solid surface is investigated comprehensively using the axisymmetric LBM with significant density and viscosity contrasts. We probe droplet impact dynamics by varying the We number, Oh number, and surface wettability. The effects of each parameter is isolated by varying the one while keeping others constant. Our results show that inertia is the most critical parameter during droplet spreading, while the recoiling is governed primarily by viscous and surface tension forces. The We number significantly influences spreading stage. The rate of recoiling depends mainly on Oh and surface wettability. Namely, faster recoil is observed at lower Oh numbers and higher equilibrium contact angles. Furthermore, the droplet on hydrophilic surfaces recoils toward the equilibrium state gradually and smoothly, while the droplet undergoes significant oscillations on hydrophobic surfaces during recoiling. As the surface wettability decreases, the time required to reach equilibrium increases. The tendency of a droplet to rebound increases by increasing We number and decreasing both Oh number and surface wettability. Velocity vector fields of impact reveal intriguing developments of circulatory flow during impact. Finally, a comparison of the droplet morphologies between axisymmetric and pure 2D LBMs indicates that the energy transfer in the 2D LBM does not capture the correct physics of 3D droplet impact, which lead to distinct impact outcomes.

Understanding droplet-solid interactions will aid in optimizing surface characteristics related to many scientific applications. For example, the total rebound of droplets from surfaces is essential in wet environments to preserve a dry surface condition and prevent corrosion. The impact dynamics also modulates heat transfer between droplet and surface, which plays a vital role in spray cooling of high power electronics and ice formation on airfoils. The axisymmetric LBM is a promising tool to elucidate fundamental physics of droplet impact in applicable conditions and provide greater hydrodynamics insight inaccessible to experimental techniques.

Acknowledgments

X.Y. acknowledges partial support from the National Science Foundation under grant No. CMMI-1538090. Computational resources were provided by the Watson Data Center at Binghamton University.

References

[1] A. L. Yarin, Annu. Rev. Fluid Mech. **38**, 159 (2006).

[2] C. Josserand and S. T. Thoroddsen, Annu. Rev. Fluid Mech. **48**, 365 (2016).

[3] R. Rioboo, C. Tropea, and M. Marengo, At. Sprays **11**, 12 (2001).

[4] H. Dong, W. W. Carr, D. G. Bucknall, and J. F. Morris, AIChE J. **53**, 2606 (2007).

[5] H. Y. Kim and J. H. Chun, Phys. Fluids **13**, 643 (2001).

[6] C. Antonini, A. Amirfazli, and M. Marengo, Phys. Fluids **24**, (2012).

[7] P. W. Wilson, W. Lu, H. Xu, P. Kim, M. J. Kreder, J. Alvarenga, and J. Aizenberg, Phys. Chem. Chem. Phys. **15**, 581 (2013).

[8] P. Kim, T.-S. Wong, J. Alvarenga, M. J. Kreder, W. E. Adorno-Martinez, and J. Aizenberg, ACS Nano **6**, 6569 (2012).

[9] L. Xiao, J. Li, S. Mieszkin, A. Di Fino, A. S. Clare, M. E. Callow, J. A. Callow, M. Grunze, A. Rosenhahn, and P. A. Levkin, ACS Appl. Mater. Interfaces **5**, 10074 (2013).

[10] X. Yao, Y. Hu, A. Grinthal, T. S. Wong, L. Mahadevan, and J. Aizenberg, Nat. Mater. **12**, 529 (2013).

[11] S. Jung, S. D. Hoath, and I. M. Hutchings, Microfluid. Nanofluidics **14**, 163 (2013).

[12] D. Bartolo, A. Boudaoud, G. Narcy, and D. Bonn, Phys. Rev. Lett. **99**, (2007).

[13] M. Aytouna, D. Bartolo, G. Wegdam, D. Bonn, and S. Rafaï, Exp. Fluids **48**, 49 (2010).

[14] L. Mishchenko, B. Hatton, V. Bahadur, J. A. Taylor, T. Krupenkin, and J. Aizenberg, ACS Nano **4**, 7699 (2010).

[15] Y. Liu, L. Moevius, X. Xu, T. Qian, J. M. Yeomans, and Z. Wang, Nat. Phys. **10**, 515 (2014).

[16] P. Tsai, S. Pacheco, C. Pirat, L. Lefferts, and D. Lohse, Langmuir **25**, 12293 (2009).

[17] C. Dorrer and J. Ruhe, Langmuir **22**, 7652 (2006).

[18] D. Richard, C. Clanet, and D. Quéré, Nature **417**, 811 (2002).

[19] J. C. Bird, R. Dhiman, H. M. Kwon, and K. K. Varanasi, Nature **503**, 385 (2013).

[20] G. H. Yeoh and J. Tu, *Computational Techniques for Multiphase Flows* (2010).

[21] A. Prosperetti and G. Tryggvason, *Computational Methods for Multiphase Flow* (2007).

[22] S. Chen and G. D. Doolen, Annu. Rev. Fluid Mech. 30329–64 **30**, 329 (1998).

[23] X. He and L.-S. Luo, Phys. Rev. E **56**, 6811 (1997).

[24] R. Benzi, S. Succi, and M. Vergassola, Phys. Rep. **222**, 145 (1992).

[25] H. Huang, M. Sukop, and X. Lu, *Multiphase Lattice Boltzmann Methods Theory and Application* (2015).

[26] T. Inamuro, T. Yokoyama, K. Tanaka, and M. Taniguchi, Comput. Fluids **137**, 55 (2016).

[27] Y. Y. Yan and Y. Q. Zu, J. Comput. Phys. **227**, 763 (2007).

[28] A. J. Briant, A. J. Wagner, and J. M. Yeomans, Phys. Rev. E - Stat. Nonlinear, Soft Matter Phys. **69**, (2004).

[29] A. J. Briant and J. M. Yeomans, Phys. Rev. E - Stat. Physics, Plasmas, Fluids, Relat. Interdiscip. Top. **69**, 9 (2004).

[30] S. Mukherjee and J. Abraham, Phys. Rev. E - Stat. Nonlinear, Soft Matter Phys. **75**, 1 (2007).

[31] a. Kuzmin, a. a. Mohamad, and S. Succi, Int. J. Mod. Phys. C **19**, 875 (2008).

[32] T. Lee and L. Liu, J. Comput. Phys. **229**, 8045 (2010).

[33] T. Lee and C. L. Lin, J. Comput. Phys. **206**, 16 (2005).

[34] I. Halliday, L. Hammond, C. Care, K. Good, and A. Stevens, Phys. Rev. E **64**, 011208 (2001).

[35] K. N. Premnath and J. Abraham, Phys. Rev. E - Stat. Nonlinear, Soft Matter Phys. **71**, (2005).

[36] S. Mukherjee and J. Abraham, J. Colloid Interface Sci. **312**, 341 (2007).

[37] K. Sun, M. Jia, and T. Wang, Int. J. Heat Mass Transf. **58**, 260 (2013).

[38] K. Connington and T. Lee, J. Comput. Phys. **250**, 601 (2013).

[39] C. E. Brennen, *Fundamentals of Multiphase Flow* (2013).

[40] X. He, S. Chen, and R. Zhang, J. Comput. Phys. **663**, 642 (1999).

[41] R. D. Schroll, C. Josserand, S. Zaleski, and W. W. Zhang, Phys. Rev. Lett. **104**, (2010).

[42] S. Bakshi, I. V. Roisman, and C. Tropea, Phys. Fluids **19**, (2007).

[43] I. V. Roisman, E. Berberović, and C. Tropea, Phys. Fluids **21**, (2009).

[44] K. Okumura, F. Chevy, D. Richard, D. Quéré, and C. Clanet, Europhys. Lett. **62**, 237 (2003).

[45] D. Richard and D. Quéré, Europhys. Lett. **50**, 769 (2000).

[46] R. M. Manglik, M. A. Jog, S. K. Gande, and V. Ravi, Phys. Fluids **25**, (2013).

[47] P. Attané, F. Girard, and V. Morin, Phys. Fluids **19**, (2007).

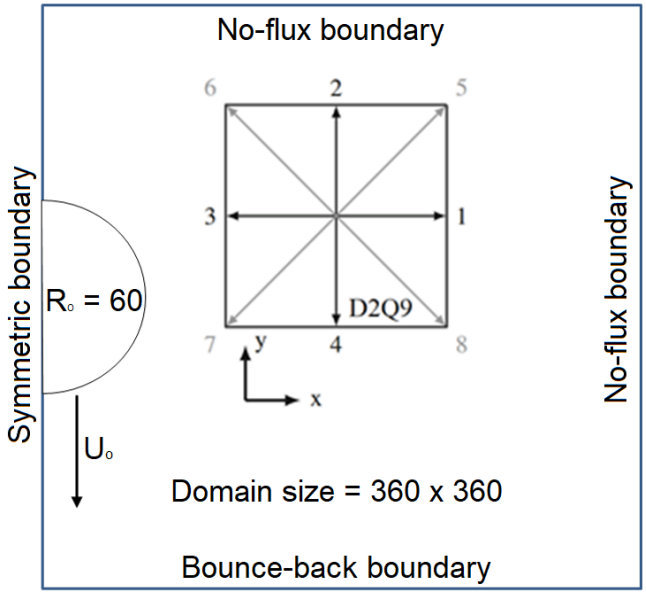

Figure (1): Schematic plot of the simulation domain used in droplet impact study.

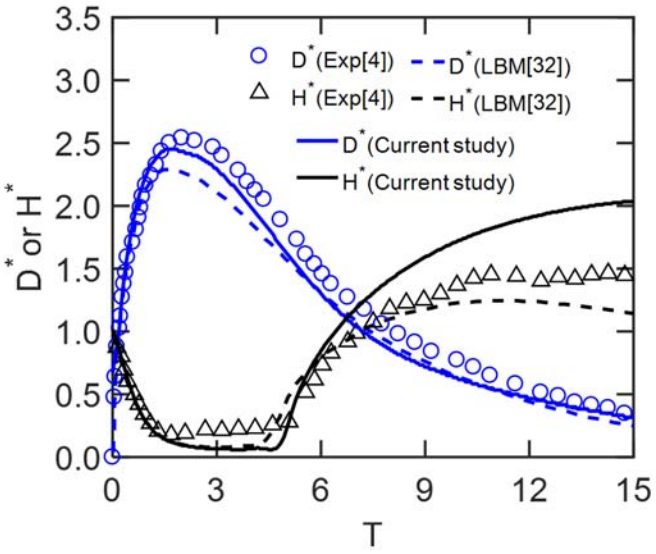

Figure (2): Comparison of droplet spreading factor (D*) and aspect ratio (H*) variations between the present study and previous experiments and simulations. The droplet normally impacts on a hydrophobic surface ($\theta^{eq} = 107^{o}$) at We = 103 and Oh = 0.015.

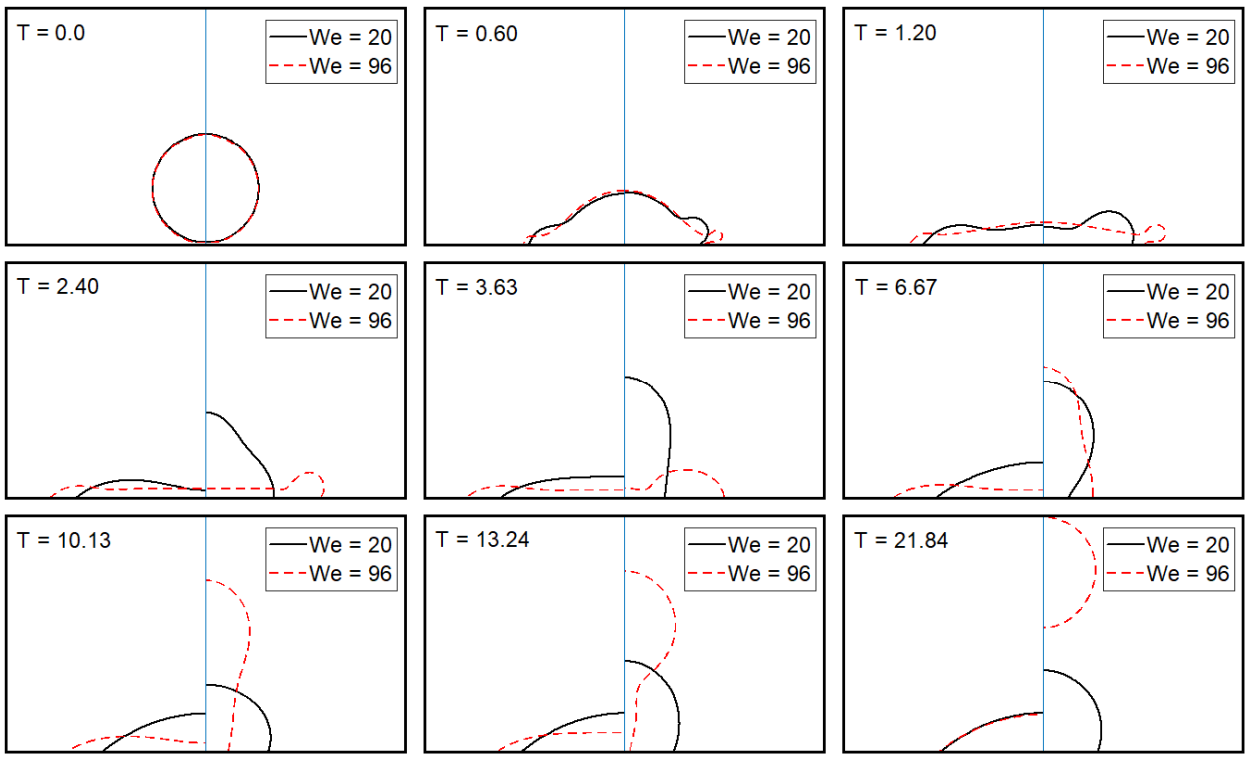

Figure (3): Instantaneous morphologies of droplet impacting at We = 20 (black solid lines) and We = 96 (red dash lines) on the solid surfaces with $\theta^{eq} = 40^{o}$ (left portion of each frame) and $\theta^{eq} = 110^{o}$ (right portion). The Oh number is fixed at 0.0218 for all simulations.

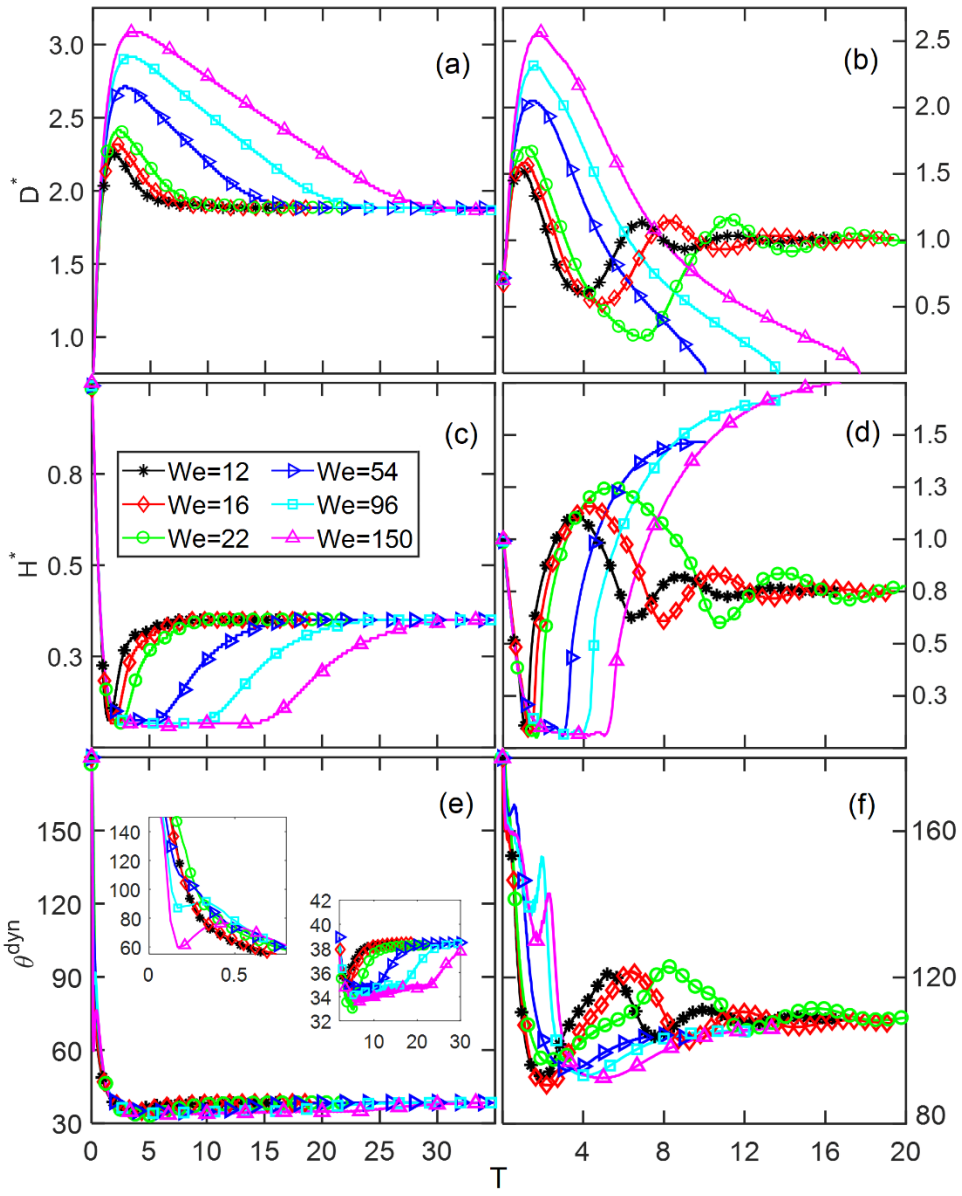

Figure (4): We-dependent variations of droplet spreading factor (upper panel), aspect ratio (middle panel), and dynamic contact angle (lower panel) in non-dimensional time at Oh = 0.0218 on hydrophilic ($\theta^{eq} = 40^{o}$ left panel) and hydrophobic ($\theta^{eq} = 110^{o}$ right panel) surfaces. The insets in (e) are the magnified views of the spreading and recoiling stages.

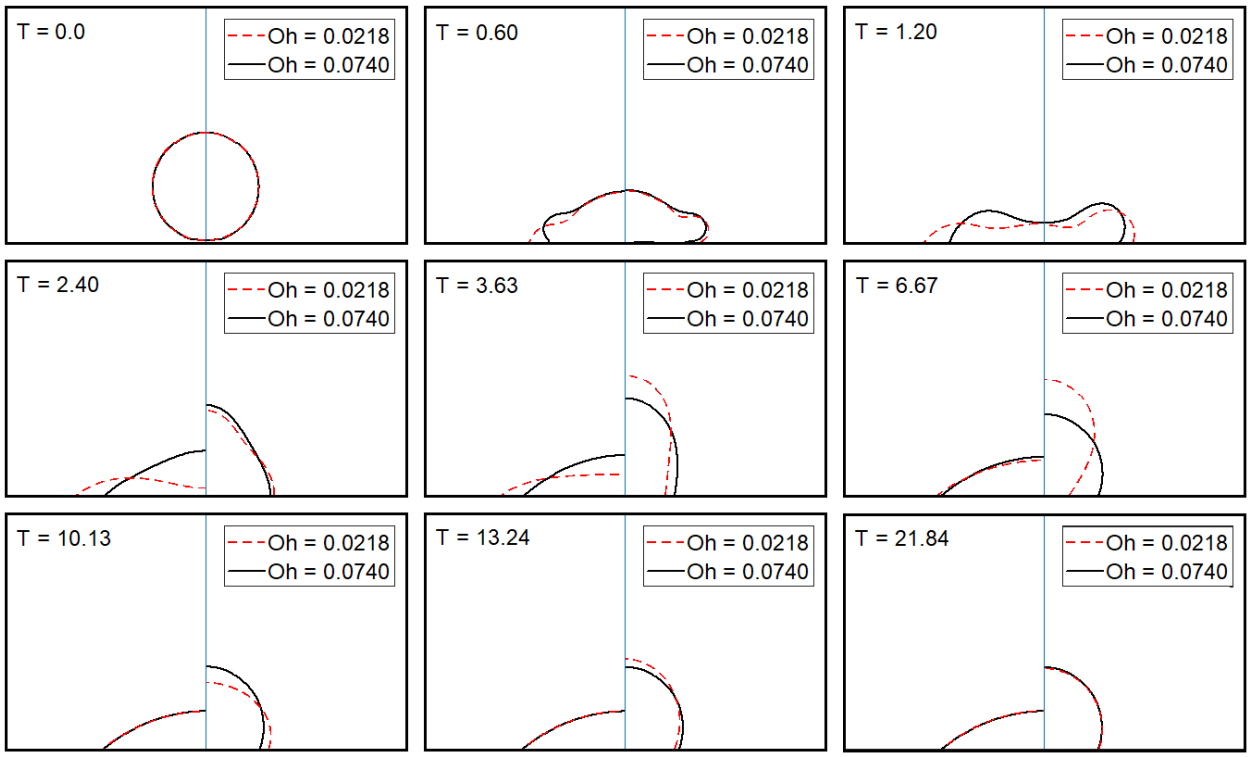

Figure (5): Instantaneous morphologies of droplet impacting at Oh = 0.0218 (red dash lines) and Oh = 0.074 (black solid lines) on the solid surfaces with $\theta^{eq} = 40^{o}$ (left portion of each frame) and $\theta^{eq} = 110^{o}$ (right portion). The We number is fixed at 20 for all simulations.

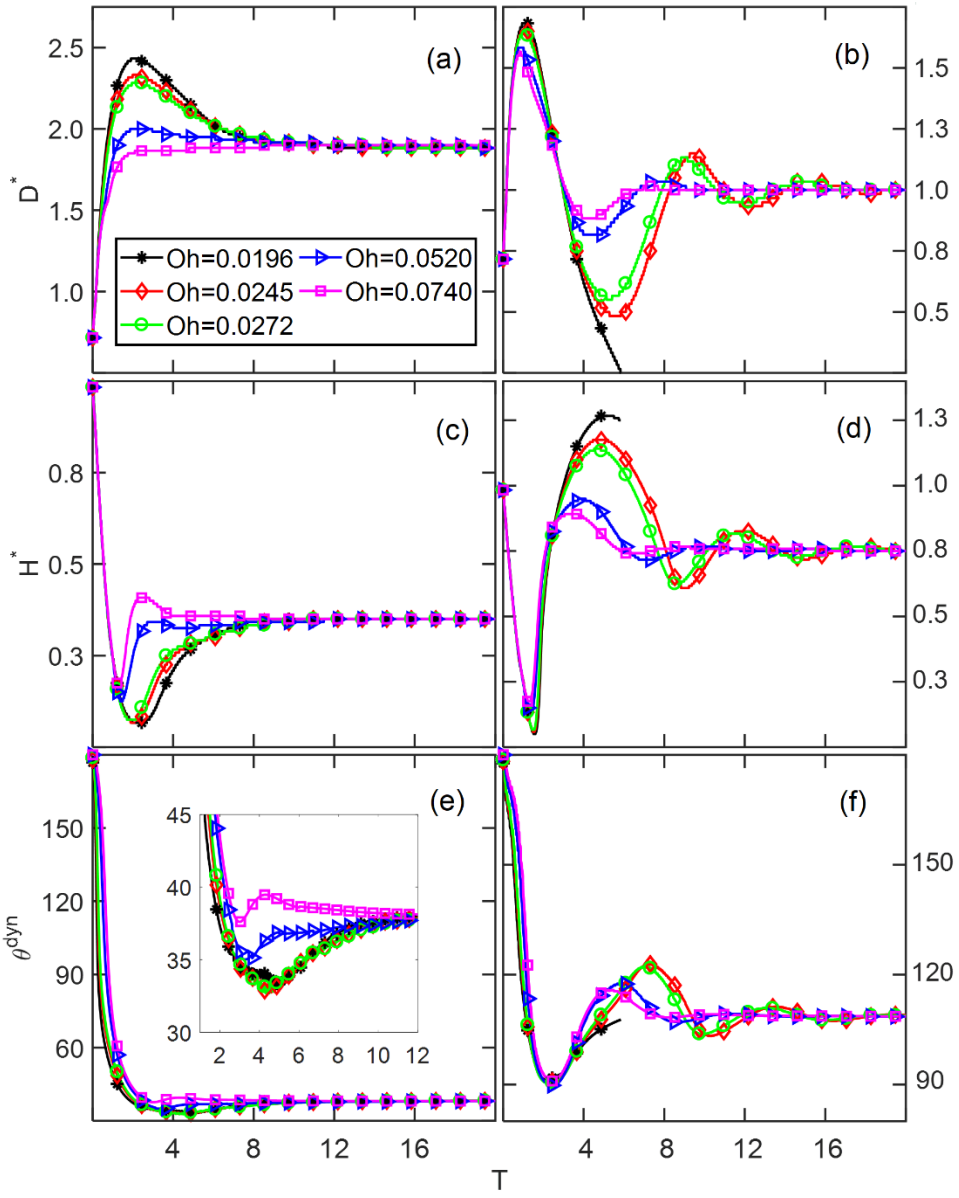

Figure (6): Oh-dependent variations of droplet spreading factor (upper panel), aspect ratio (middle panel), and dynamic contact angle (lower panel) in non-dimensional time at We = 20 on hydrophilic ($\theta^{eq} = 40^{o}$ left panel) and hydrophobic ($\theta^{eq} = 110^{o}$ right panel) surfaces. The inset in (e) is the magnified view of the recoiling stage.

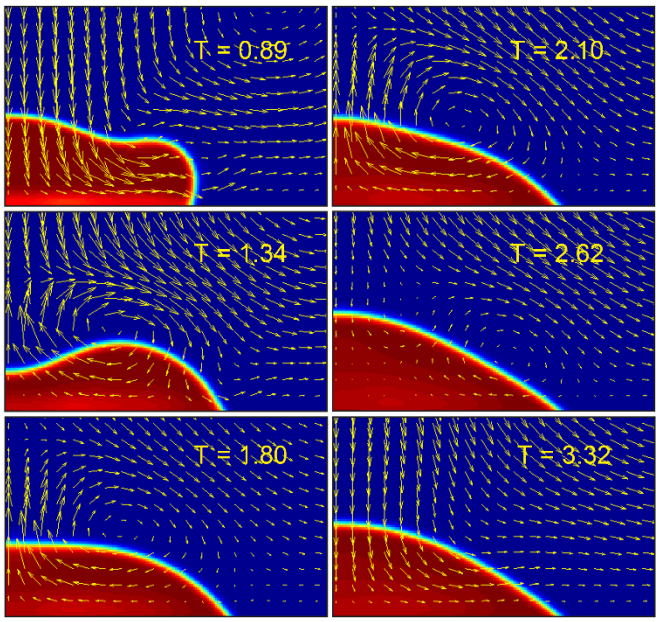

Figure (7): Instantaneous velocity vector fields of droplet impacting on a hydrophilic solid surface ($\theta^{eq} = 40^{o}$) at We = 20 and Oh = 0.074.

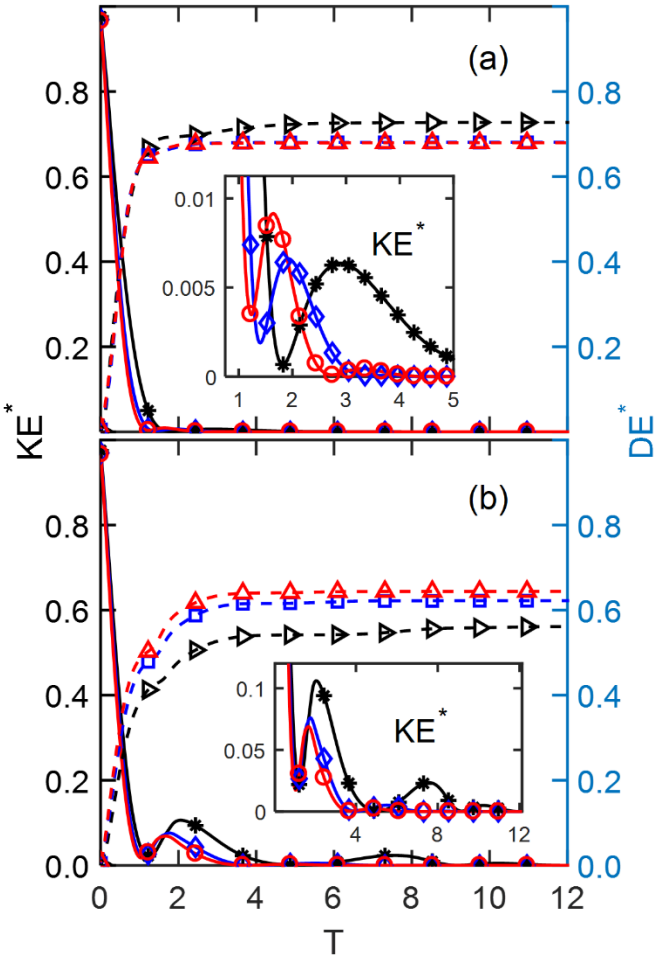

Figure (8): Normalized kinetic energy and viscous dissipation energy of the droplet versus non-dimensional time at various Oh numbers on (a) hydrophilic, $\theta^{eq} = 40^{o}$ and (b) hydrophobic, $\theta^{eq} = 110^{o}$ surfaces. The insets are the detailed views of the normalized kinetic energy variation. The We number is fixed at 20 for all simulations. The symbols are ✱, ◇ and ○ respectively for KE* at Oh = 0.0245, 0.0520 and 0.0740. while the symbols ▷, □ and △ respectively for DE* at Oh = 0.0245, 0.0520 and 0.0740.

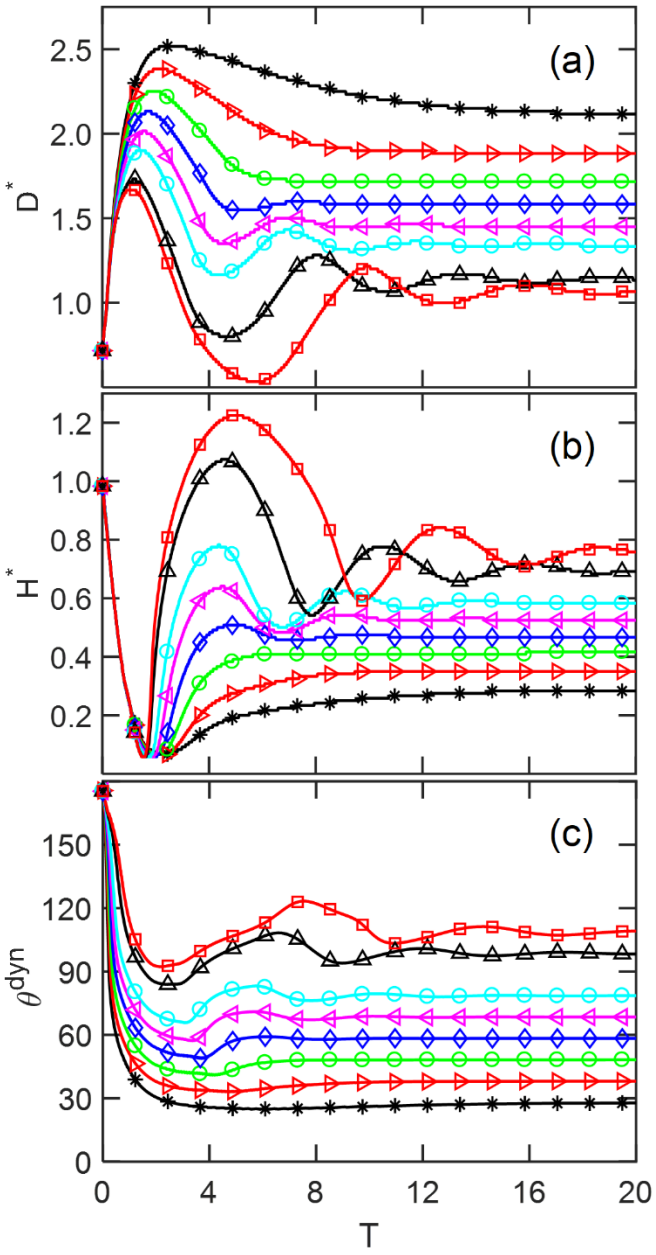

Figure (9): (a) Spread factor, (b) aspect ratio, and (c) dynamic contact angle versus non-dimensional time at We = 20, Oh = 0.0218 for different equilibrium contact angles. The symbols are ✱, ▷, ○, ◇, ◁, ●, △ and □ respectively for $\theta^{eq} = 30^{o}$, 40^{o} , 50^{o} 60^{o} 70^{o} 80^{o} 100^{o} and 110^{o} .

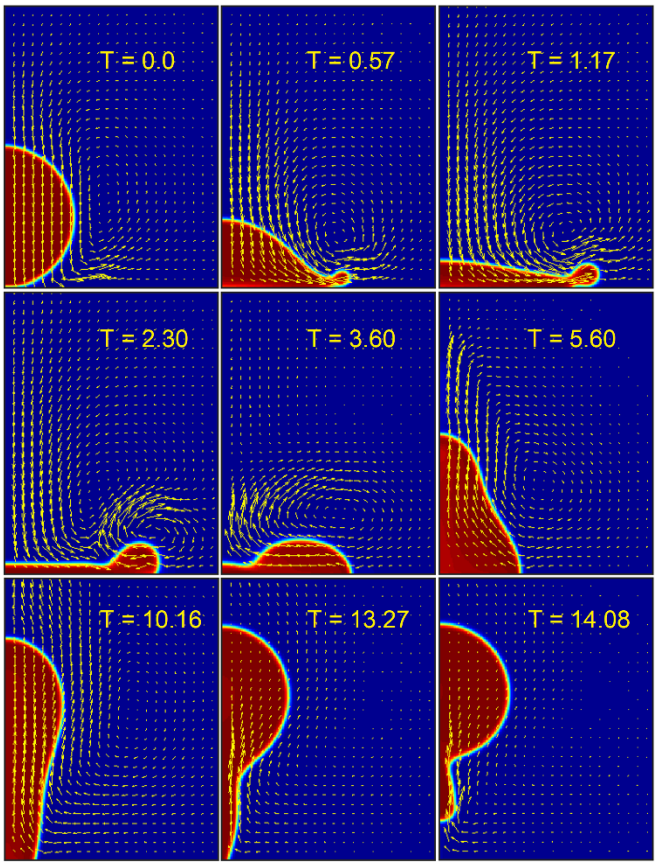

Figure (10): Instantaneous velocity vector fields of droplet impacting on a hydrophobic solid surface ($\theta^{eq} = 110^{o}$) at We = 96 and Oh = 0.0218.

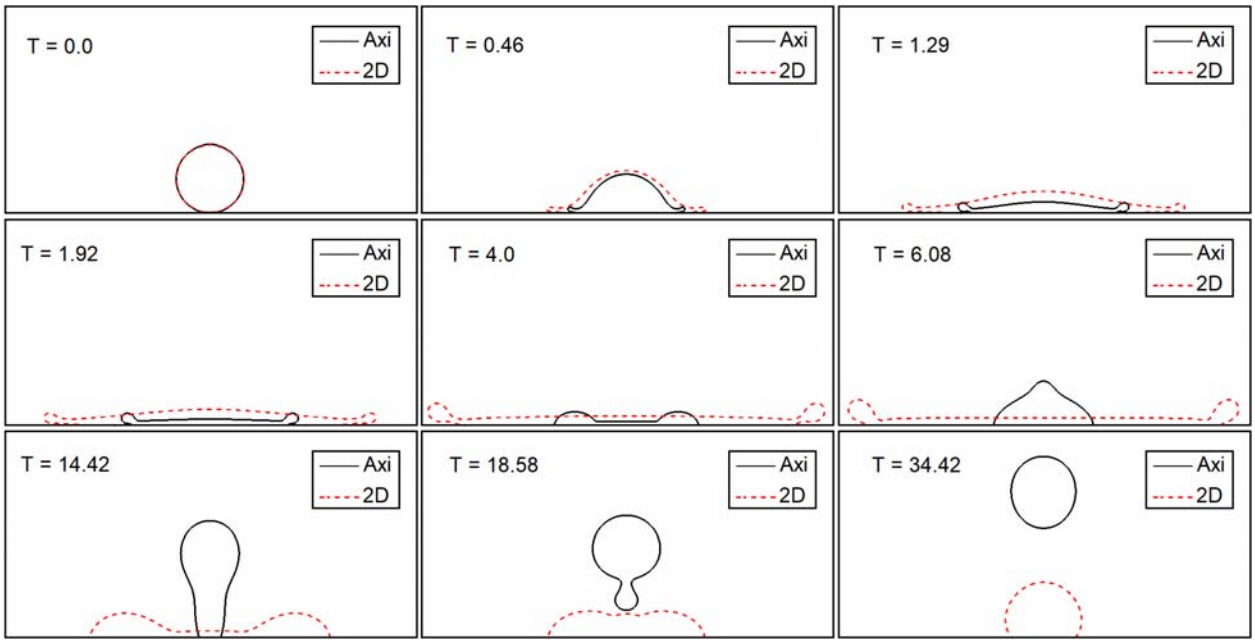

Figure (11): Droplet morphology comparison between axisymmetric and 2D LBMs at We = 20, Oh = 0.0218, and $\theta^{eq} = 110°$.